

DEEP CFHT Y-BAND IMAGING OF VVDS-F22 FIELD: II. QUASAR SELECTION AND QUASAR LUMINOSITY FUNCTION

JINYI YANG^{1,2}, XUE-BING WU^{1,2}, DEZI LIU¹, XIAOHUI FAN^{3,2}, QIAN YANG^{1,2}, FEIGE WANG^{1,2}, IAN D. MCGREER³, ZUHUI FAN¹, SHUO YUAN¹, HUANYUAN SHAN^{4,5}

Draft version November 15, 2021

ABSTRACT

We report the result of a faint quasar survey in a one square degree field. The aim is to test the $Y - K/g - z$ and $J - K/i - Y$ color selection criteria for quasars at faint magnitude, to obtain a complete sample of quasars based on deep optical and near-infrared color-color selection, and to measure the faint end of quasar luminosity function (QLF) over a wide redshift range. We carried out a quasar survey based on the $Y - K/g - z$ and $J - K/i - Y$ quasar selection criteria, using the deep Y-band data obtained from our CFHT/WIRC*am* Y-band images in a two-degree field within the F22 field of the VIMOS VLT deep survey, optical co-added data from Sloan Digital Sky Survey Stripe 82 and deep near-infrared data from the UKIDSS Deep Extragalactic Survey in the same field. We discovered 25 new quasars at $0.5 < z < 4.5$ and $i < 22.5$ mag within one square degree field. The survey significantly increases the number of faint quasars in this field, especially at $z \sim 2 - 3$. It confirms that our color selections are highly complete in a wide redshift range ($z < 4.5$), especially over the quasar number density peak at $z \sim 2 - 3$, even for faint quasars. Combining all previous known quasars and new discoveries, we construct a sample with 109 quasars, and measure the binned QLF and parametric QLF. Although the sample is small, our results agree with a pure luminosity evolution at lower redshift and luminosity evolution and density evolution model at redshift $z > 2.5$.

Subject headings: galaxies: active - galaxies:high-redshift - quasars: general - quasars: emission lines

1. INTRODUCTION

Quasar luminosity function (QLF) has been the most important tool to directly characterize the evolution of quasar number density with redshift and luminosity for a half century. The measurement of QLF highly depends on the sample of quasars. Quasar samples currently available are usually incomplete due to various problems (e.g. photometry depth, instruments limitation), especially in the quasar candidate selections (Richards et al. 2002). For example, both 2dF QSO Redshift Survey (Boyle et al. 2000) and Sloan Digital Sky Survey (SDSS) (e.g. DR7 quasar catalog; Schneider et al. 2010) adopted UV excess-based technique to select $z < 2.2$ quasars. More recent surveys focusing on quasars at $z \sim 2 - 3$ and higher redshifts have improved quasar samples at these redshifts (Ross et al. 2012; Myers et al. 2015). The SDSS-III Baryon Oscillation Spectroscopic Survey (BOSS, Dawson et al. 2013; Ross et al. 2012) highly improved quasar selection at $z > 2.2$ and spectroscopically identified $\sim 170,000$ new quasars at $2.1 < z < 3.5$ to the depth of $g < 22$. The SDSS IV extended Baryon Oscillation Spectroscopic Survey (eBOSS, Dawson et al. 2016; Myers et al. 2015) adopting two approaches, one from the combination of likelihood-based selec-

tion with mid-IR-optical color cut, the other one from variability, aims at targeting more quasars at $z > 2.2$. While, the current $z \sim 2 - 3$ quasar surveys are still not highly complete. Because the selections, in color space, always need to avoid the whole region that is seriously contaminated by stars.

Based on the previously suggested K -band excess technique (Hewett et al. 2006; Maddox et al. 2008; Warren et al. 2000), Wu & Jia (2010) posed two new selection criteria involving both optical and near-infrared (NIR) colors for selecting quasars at $z < 4$ and $z < 5$, respectively. They found that quasars at redshift $z < 4$ could be separated from stars well in the $Y - K$ versus $g - z$ color-color diagram, while quasars at $z > 4$ begin to enter the loci of stars due to the shift of strong Ly α emission line. In this case, the $J - K/i - Y$ color-color diagram has been suggested as effective in separating quasars at $4 < z < 5$ from stars. Wu & Jia (2010) cross-matched SDSS DR7 quasar catalog with the UKIRT InfraRed Deep Sky Surveys (UKIDSS) (Casali et al. 2007; Hewett et al. 2006; Lawrence et al. 2007) DR3 NIR photometric data to obtain a sample of 8498 quasars with both SDSS and UKIDSS photometry. They tested the $Y - K/g - z$ and $J - K/i - Y$ selection criteria with this quasar sample, and found that the $Y - K/g - z$ color cut could select 98.6% of $z < 4$ known quasars, and $J - K/i - Y$ cut could recover 97.5% of $z < 4$ quasars, and 99% of $4 < z < 5$ quasars. Some spectroscopic observations carried out by Wu et al. (2010a,b) and Wu et al. (2011) have also demonstrated the effectiveness of using the SDSS-UKIDSS optical/NIR colors to find SDSS missing quasars at $2.2 < z < 3.5$. Therefore, these selection criteria are expected to be helpful for the construction of a relatively more complete quasar sample at $z < 5$, especially at the range of $2 < z < 3$. In addition, Wu &

¹ Department of Astronomy, School of Physics, Peking University, Beijing 100871, China

² Kavli Institute for Astronomy and Astrophysics, Peking University, Beijing 100871, China

³ Steward Observatory, University of Arizona, 933 North Cherry Avenue, Tucson, AZ 85721, USA

⁴ Argelander-Institut für Astronomie, Auf dem Hügel 71, 53121 Bonn, Germany

⁵ Laboratoire d'astrophysique (LASTRO), Ecole Polytechnique Fédérale de Lausanne (EPFL), Observatoire de Sauvigny, CH-1290 Versoix, Switzerland

Jia (2010) only tested their selection criteria with relative bright quasar sample. A fainter sample is necessary to test this selection method at faint end.

Therefore, to construct a more complete quasar sample at $z < 4$, especially at the faint end, we used these two selection criteria to select quasar candidates in a deep optical/NIR surveyed field. VVDS F22 is a wide field covering a sky area of 4 square degrees (Garilli et al. 2008; Le Fèvre et al. 2013). This field was mapped by the VIMOS VLT deep survey (VVDS) deep optical (U,B,V,R,I) and NIR (*J,K*, but restricted access) photometry, which reached the depth of $I \sim 25$ mag and $K \sim 23$ mag (AB). It was also covered by the SDSS stripe 82 (Annis et al. 2014) deep optical photometry, CFHT Legacy Survey (CFHTLS), the UKIDSS - Large Area Survey (LAS) & Deep Extragalactic Survey (DXS), and NRAO Very Large Array Sky Survey (NVSS) (Condon et al. 1998). Since there is no existing deep Y-band photometry, we first obtained deep Y-band image in this field and then carried out a small field but deep quasar spectroscopic survey. VVDS spectroscopy has been done with a sampling rate of 22% for sources with $I < 22.5$, and has obtained the spectra of 11228 galaxies, 6748 stars and 167 quasars (Garilli et al. 2008; Le Fèvre et al. 2013). With new deep Y-band photometric data, we will be able to construct a more complete quasar sample. This sample will also enable the measurement of the faint end of QLF.

In this paper, we report our work on a faint quasar survey based on our deep Y-band imaging in a square degree field of VVDS F22. We will describe the Y-band imaging and quasar candidates selection in Section 2. The spectroscopic observations, new discoveries and the construction of a quasar sample will be presented in Section 3. In Section 4 and 5, we will discuss the completeness of our survey and measure the QLF in a one square degree field. We adopt a Λ CDM cosmology with parameters $\Omega_\Lambda = 0.728$, $\Omega_m = 0.272$, $\Omega_b = 0.0456$, and $H_0 = 70 \text{ km s}^{-1} \text{ Mpc}^{-1}$ (Komatsu et al. 2009). Photometric data from the Sloan Digital Sky Survey (SDSS) are in the SDSS photometric system (Lupton et al. 1999), which is almost identical to the AB system at bright magnitudes; photometric data from NIR surveys are in the Vega system.

2. CANDIDATES SELECTION

2.1. Deep Y-band photometry

We obtained Y-band imaging of a two square degree field (see Fig.1) within F22 field of the VVDS using CFHT WIRCam in August, September and October, 2012. The WIRCam focal plane is made of a mosaic which includes four HAWAII2-RG detectors. The field of view of the full mosaic is $21.5' \times 21.5'$. We divided our two square degree field into 18 sub-fields, each of $20' \times 20'$, as shown in Figure 1. The final imaged area is about $128' \times 65'$, fully covering those 18 sub-fields. More details of Y-band imaging can be found in Liu et al. (2017), including observation, data reduction, data release and Y-band related photometric redshift measurements.

The Y-band photometric data used in this paper for quasar survey was the earlier version (in 2013) of the finally published data (in 2017). The deep Y-band image was processed by SIMPLE-WIRCAM pipeline Wang et

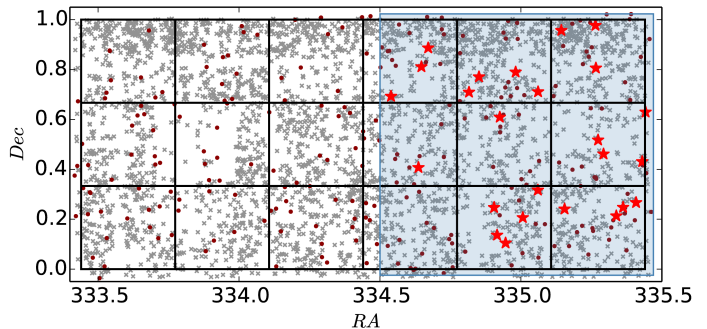


FIG. 1.— Sky coverage of the deep Y-band image. The black frames represent 18 sub-fields, each of $20' \times 20'$. The final imaged area is about $128' \times 65'$. The dark red dots and grey crosses denote spectroscopically identified quasars and galaxies by previous works (e.g. SDSS DR7, 9, 10, 12 quasar catalog and VVDS spectroscopy; Schneider et al. 2010; Pâris et al. 2012, 2014, 2017; Garilli et al. 2008; Le Fèvre et al. 2013). The shaded region represents the area of our spectroscopy survey, and new quasars from our survey are marked as red stars.

al. (2010) specified for CFHT/WIRCAM image analyses. The basic steps of CFHT/WIRCAM image reduction encoded in the pipeline contains flat-fielding, sky subtraction, cosmic ray removal, astrometric calibration and final image stacking. We used SExtractor (Bertin & Arnouts 1996) and DAOPHOT for source extraction and photometry (aperture photometry by DAOPHOT). In total, ~ 110000 sources were detected within this field. The final Y-band photometric data has been published by Liu et al. (2017), which was an improved version for photometric redshift measurements (e.g. PSF homogenization of different bands). The 5σ magnitude limit of Y-band photometry is 22.25 mag in Vega magnitude system.

2.2. Quasar candidate selection

We started our selection with the catalog of deep Y-band detected sources in the region of $333.40^\circ \leq RA \leq 335.47^\circ$ and $-0.05^\circ \lesssim Decl. \lesssim 1.024^\circ$. We cross matched ($3''$) the Y-band source catalog with the co-added SDSS Stripe 82 catalog from Annis et al. (2014)⁶ and UKIDSS UDXS DR9 catalog to obtain required photometric data in *g, i, z, Y, J* and *K* bands. We obtained a sample of $\sim 105,000$ sources.

Since our selection focused on faint objects, galaxy contamination is serious. We use SDSS data for star/galaxy separation. Our two square degree field was covered by SDSS Stripe82 photometry, which is a 275 square degree region on the Celestial Equator in the Southern Galactic Cap. This region was imaged multiple times by SDSS *u, g, r, i, z* bands during the fall seasons when the North Galactic Cap was not observable. After a co-addition of multiple epoch images, Stripe82 data reaches a depth more than 2 magnitude fainter than the SDSS main survey and a $\sim 1.1''$ median seeing in *r* band (Annis et al. 2014). The stringent point/extended separator used by Stripe 82 data release, $|r_{psf} - r_{model}| \leq 0.03$, could significantly reduce the number of misclassified galaxies, comparing with the SDSS standard star/galaxy separation ($|r_{psf} - r_{model}| \leq 0.145$). But when testing with a sample of previously known quasars, we found this sepa-

⁶ The final catalog was published in 2014. But we used the older version of catalog from Annis et al. (2011, arXiv: 1111.6619v2) when we selected candidates in 2013.

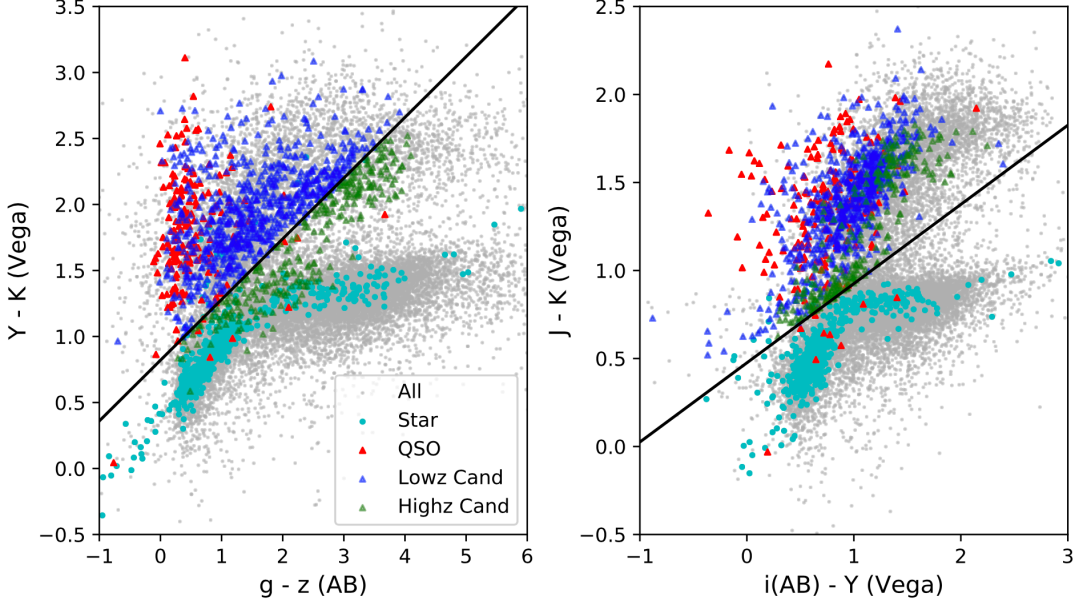


FIG. 2.— The $Y - K/g - z$ and $J - K/i - Y$ color-color diagrams and cuts used to select quasar candidates from all point sources. The grey points represent all sources within this field. The previously known quasars (red triangles), stars (cyan dots) are also plotted. Sources met $Y - K/g - z$ or $J - K/i - Y$ color-based selection criteria were denoted by blue triangles (low redshift quasar candidates) and green triangles (high redshift quasar candidates).

ration would misclassify some faint or low redshift known quasars. So to improve the completeness of quasar selection, we need to relax the separation. We used a sample of Stripe 82 detected previously known quasars, stars and galaxies to draw a new cut, $|r_{psf} - r_{model}| \leq 0.1$. This cut help us to selected $\sim 40,000$ sources from the whole sample.

We selected quasar candidates from all point sources by using the $Y - K/g - z$ and $J - K/i - Y$ selection criteria. The selection criteria we used are listed below. We also limited the magnitude errors of g, i, z bands to be smaller than 0.5 and image quality flags of Y, J, K bands to be 0, which mean clean photometry. The J/Kflags (also named as jppErrBits and kppErrBits) were obtained from UKIDSS UDXS DR9. The J/Kflags is the post-processing error quality bit flags assigned in the Wide Field Camera Science Archive (WSA) curation procedure for survey data. A J/Kflags > 0 represents bad image quality (e.g. blended, bad pixel(s) in default aperture, close to saturated). The Y-band image flag was set by our data reduction in the same way to UDXS data. Considering the flux limit of MMT spectroscopic observation and the limited exposure time, we select objects with i band magnitude brighter than 22.5 mag. When we selected candidates for spectroscopy, we required that the object meets equations (1) - (4), and then either (5)&(6) or (7)&(8). Since the $Y - K/g - z$ cut focuses on quasars at $z < 4$ and $J - K/i - Y$ can recover most of quasars at $4 < z < 5.3$, we also marked candidates that met $J - K/i - Y$ selection but not $Y - K/g - z$ as high redshift quasar candidates. Here, the i band magnitude used in the $J - K/i - Y$ color-color cut (eq. 7) has been converted to Vega magnitude by $i_{Vega} = i_{AB} - 0.366$. The color - color diagrams are plotted in Fig 2. As shown, the color cuts can recover most of previously known quasars. All optical data used for color-color cuts are corrected

for Galactic extinction. After color-color selection, we restricted candidate sample to $\sim 1,300$ sources.

$$i < 22.5; \quad (1)$$

$$Yflag = 0; \quad (2)$$

$$Jflags = 0; \quad (3)$$

$$Kflags = 0; \quad (4)$$

and

$$Y - K > 0.46(g - z) + 0.82 \quad (5)$$

$$err_g < 0.5 \text{ and } err_z < 0.5 \quad (6)$$

or

$$J - K > 0.45(i - Y) + 0.475 \quad (7)$$

$$err_i < 0.5 \quad (8)$$

We then used a χ^2 estimations to further rejects star contaminations from the color selected candidate sample. The χ^2 represents a χ^2 fitting of each object's photometric data to the quasar color-z relations (Wu & Jia 2010; Yang et al. 2017). The quasar color-z relation was generated by using a sample of real quasars. We first calculated the mean colors at each redshift bin and rejected quasars with any color out of 3σ to the mean value. Then we constructed the color-z relation using remaining quasars. Following the method given by Weinstein et al. (2004), we calculated the mean color vector M_i and the covariance matrix V_i in the i th redshift bin. For each candidate, based on its photometric data, we could get the magnitude error matrix V_0 . Then we computed the χ^2 value between the colors of candidate and color-z relation in the i th redshift bin: $\chi_i^2 = (X_0 - M_i)^T (V_0 + V_i)^{-1} (X_0 - M_i)$, where the vector X_0 represents the observed colors of a candidate (Weinstein et al. 2004). From this χ^2 value, we could derive

the probability that a candidate lay in the i th redshift bin. But here we only used the minimum χ^2 value of a candidate for star/quasar separation. Photometric data in u, g, r, i, z, Y, J and K bands were involved in the χ^2 calculation.

A smaller χ^2 value means that the colors of this source are more similar to the quasar colors at a given redshift than star's colors. Thus this source is expected to have higher probability to be a quasar. We tested the fitting by using spectroscopically identified quasars and stars and found that the χ^2 of most quasars were relatively smaller than that of stars. So we can define a χ^2 cut to separate quasars and stars. Generally, a higher χ^2 limit corresponds higher quasars selected fraction (high completeness) but also higher fraction of stars contamination (low efficiency). We finally used the limit of χ^2 value less than 15 to separate quasar from star, which is an empirical cut generated based on the χ^2 distribution of known quasars and stars.

Based on the selections described above, after removing all previously known objects, we finally selected about 550 quasar candidates in the two square degree field. All quasar candidates were also divided into three parts and set as different ranks. Candidates with different ranks had different priorities to be targeted and observed. The first rank with highest priority included candidates with smaller χ^2 value (< 10). The second rank represented candidates with larger χ^2 value (> 10) but better morphology ($|r_{psf} - r_{model}| \leq 0.03$), and remaining candidates were marked as rank 3. There are ~ 290 rank 1 candidates, ~ 100 rank 2 candidates and ~ 160 rank 3 candidates.

3. RESULTS

3.1. Observations

Our quasar candidates were observed by MMT/Hectospec (Fabricant et al. 2005). We divided our two square degree field into two 1 square degree fields to match the Hectospec focus plane. Considering the fibers density and the efficiency of fiber configuration ($\sim 70\% - 80\%$), we finally submitted our quasar candidates together with about 240 galaxy candidates which were related with another project. When we did fiber allocation, we chose a configuration that could target more candidates in the first rank. After fiber fitting, 280 quasar candidates were targeted by MMT Hectospec. Our spectroscopically identifications have been done on October 8, 9 and November 29, 2013 with MMT Hectospec in a one square degree field ($334.5^\circ < RA < 335.47^\circ$). In this one square degree field, 143 quasar candidates had been observed. Candidates in the other one square degree field were not observed due to the limited observing time. The effective exposure time for final identification is 3×30 minutes in total with an average seeing $\sim 0.52''$.

3.2. New Quasars

We reduced all MMT/Hectospec spectra using the IDL pipeline HSRED v2.0⁷. We used Stripe 82 r band photometric data for absolute flux calibration. As a comparison, we re-observed three previously known SDSS

quasars. From a comparison between MMT spectra and SDSS spectra, we believe that the slope, wavelength and flux calibration of our MMT spectra are reasonable. We measure the redshifts by visually matching the observed spectrum to quasar template using an eye-recognition assistant for quasar spectra software ASERA (Yuan et al. 2013). This matching is based on broad emission lines of Ly β , Ly α , N V, O I/Si II, Si IV, C IV, C III and Mg II. The typical uncertainty of our redshift measurement is around 0.03. We finally obtain 25 new quasars with $0.6 < z < 4.3$. The MMT/Hectospec spectra of these new quasars are shown in Figure 3. Other candidates without broad emission lines can not be identified as quasar. The signal-to-noise ratio of those spectra are also not high enough for specific stellar types. Typically, the main contaminations for $z \sim 2 - 3$ quasars are A and F stars. Since we did not strictly limit the magnitude errors, large photometric errors will broaden the stellar locus and thus the contamination rate will be high. In addition, we relaxed star/galaxy separation to cover more quasars, so compact galaxy will also be a factor.

3.3. A uniformly selected quasar sample

Combining our new discoveries and previously known quasars, we construct a uniform sample of quasars at $0.5 < z < 4.5$ within this 1 square degree field. We restrict the area to: $334.50^\circ \leq RA \leq 335.47^\circ$ and $-0.025^\circ \leq Decl. \leq 1.023^\circ$, a 1.02 square degree field. In this region, there are 114 previously known quasars in total in the redshift range of $0.5 < z < 4.5$, mainly from SDSS DR7, DR9 & DR10 and VVDS spectroscopy (Schneider et al. 2010; Páris et al. 2012, 2014, 2017; Garilli et al. 2008; Le Fèvre et al. 2013). Four quasars were not detected by deep Y -band, Stripe 82 or UDXS photometry. The two missed by Y -band image located near the edge of image or in a masked region. In Figure 4, we plot the redshift distribution of all quasars in this field detected by Stripe 82, Y -band and UDXS photometry, including 110 known quasars and our new discoveries. As shown, our work has added a significant number of quasars at $z \sim 2$, which is one of the goals of our survey. Among those 110 known quasars, 107 quasars are brighter than our magnitude limit. All of these 107 quasars are selected by our color-color selection criteria. It also confirms the high completeness of our color-color selection which can cover a wide redshift range from 0.5 to 4, especially over the highly contaminated redshift range at $2 < z < 3$. Comparing with BOSS (Ross et al. 2012, 2013), our color-color criteria yield higher completeness by involving only g, i and z bands in optical and adding NIR colors.

There are 10 previously known quasars rejected by point/extended separator, 12 quasars rejected by χ^2 limit, and another one quasar rejected by both. Our relaxed limit on magnitude errors will result in a lower successful rate but higher completeness of color-color selection. While objects with large photometric errors may be rejected by χ^2 estimator since larger photometric error will lead to a larger χ^2 value. The completeness of selection pipeline will be quantified in next Section. Our final uniformly selected quasar sample includes 109 quasars at $0.5 < z < 4.5$. By counting all selected known quasars and our new discoveries, we can estimate a contamination rate of our selection. There were 365 objects selected by

⁷ [git://github.com/richardjcool/HSRed.git](https://github.com/richardjcool/HSRed.git)

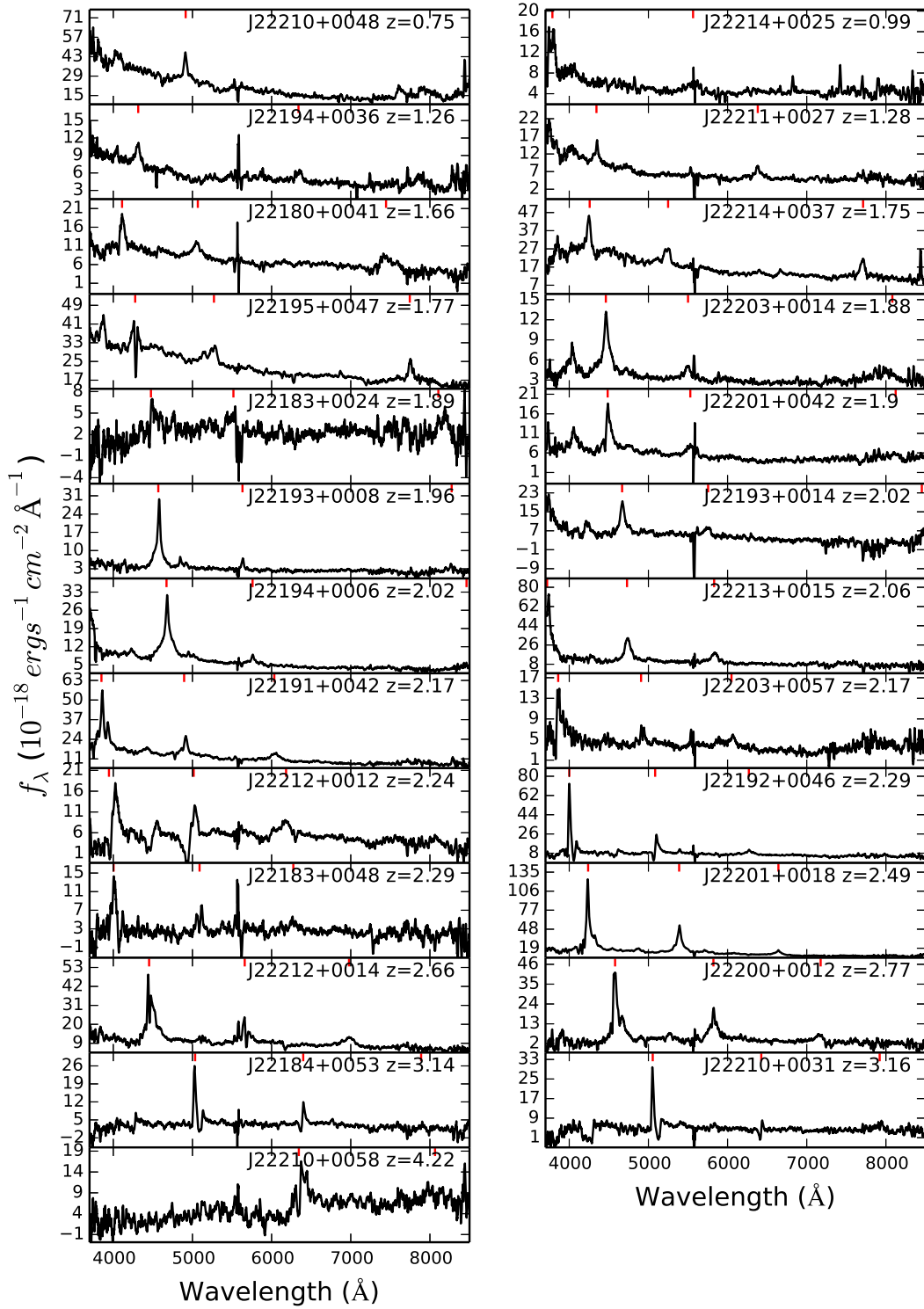


FIG. 3.— The spectra of 25 newly discovered quasars in the one square degree field. They are smoothed with 15 pixel ($1.21\text{\AA}/\text{pixel}$) box char. The red vertical lines show the Ly α , C IV and Mg II emission lines. All spectra are corrected for Galactic extinction using the Cardelli et al. (1989) Milky Way reddening law and $E(B - V)$ derived from the Schlegel et al. (1998) dust map.

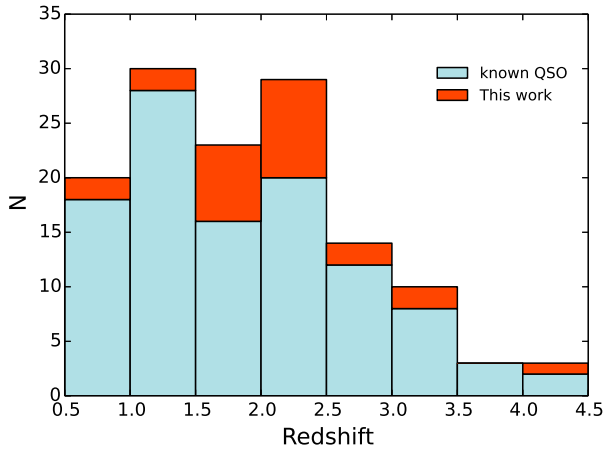


FIG. 4.— Redshift distribution of newly discovered quasars and 110 previously known quasars. Our survey mainly contributes to the quasar distribution at $z \sim 2$.

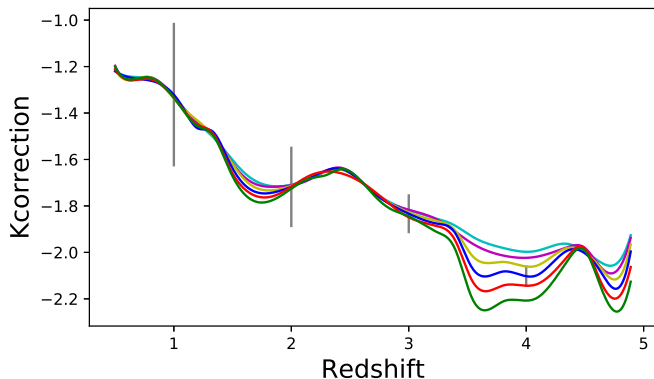


FIG. 5.— k correction used to convert apparent i band magnitude to absolute magnitude M_{1450} . We plot them in different i band magnitude bins from $\langle i \rangle = 17.5$ (cyan) to 22.5 (green) in the step of $\Delta m = 1$. The magnitude-dependent k correction is caused by the luminosity-dependent equivalent width of emission line. The gray vertical lines represent scatter of k correction at redshift $z = 1, 2, 3, 4$, generated by calculating standard deviation of k corrections in simulated spectra.

our selection in this field, including 84 previously known quasars and our 281 candidates. Through the Hectospec observation, we observed 143 candidates and obtained 25 new quasars among 281 candidates. After applying the incompleteness correction of spectroscopy (See Sec. 4), we estimate that the number of expected quasars selected by our selection in this field is 130 in total. Therefore, we obtain a 64.4% ($1 - 130/365$) contamination rate of our selection method.

We calculate the absolute AB magnitude at the rest-frame 1450Å M_{1450} of all 109 quasars using k correction determined by using a sample of simulated quasar spectra. The simulated quasar sample is built based on quasar template with scatters of continuum slope and equivalent width of emission lines. This sample is what we use for the estimation of selection function in Section 4.1, where we will describe in more details. The k

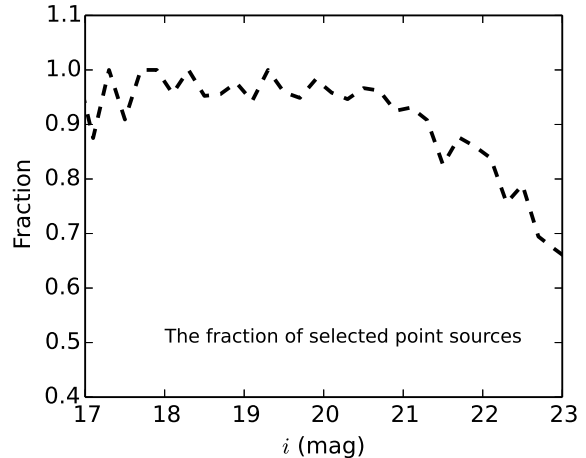


FIG. 6.— The completeness of point/extend source separation from i band magnitude 17 to 23 mag. It is a function of i band magnitude.

correction shows dependence on luminosity at some redshifts due to the luminosity-dependent equivalent width of emission line, e.g. the Baldwin effect (Baldwin 1977). Since we use i band apparent magnitude to estimate M_{1450} , we generate an i band magnitude-dependent k correction. Using simulated quasars, we produce k -correction curves from i band apparent magnitude to M_{1450} at the redshift range of $0.5 < z < 4.5$, by calculating the mean value of k correction at each redshift and i band magnitude bins ($\Delta z = 0.01$, $\Delta i = 0.01$), as shown in Figure 5. In Figure 5, we can see that the largest difference in k correction between different magnitude bins is at the redshift range of $3.5 < z < 4.4$, when C IV line moves into i band. At $z > 4.6$, the i band magnitude is significantly affected by Ly α emission line, although Ly α somewhat shows weaker Baldwin effect than C IV (Peterson 1997). The difference shown at $z \sim 1.6$ represents the effect from Mg II. We list redshifts, M_{1450} and photometry information of 109 quasars in Table 1. All optical data have been corrected for Galactic extinction.

4. SELECTION FUNCTION

In this section, we will describe the completeness of our selection pipeline, including photometry detection, point/extend source separation, color-color cuts, χ^2 limit, and spectroscopy. As discussed above, there are 4 of 114 quasars missed by deep Y -band, Stripe 82 or UDXS photometry. So we directly use this fraction as the detection incompleteness of the Stripe 82- Y -UDXS photometric data set we used, by assuming that the candidate sample has missed the same fraction of quasars to known quasars.

The completeness of point/extended source separation is expected to be a function of brightness. We determine the completeness by using a sample of HST imaged point sources. These point sources are required to locate within Stripe 82 covered areas which have similar observing condition and image quality to our one square degree field. Based on Figure 4, 5 and 6 in Annis et al. (2014), we choose the area in the range of $0^\circ < Decl. < 1^\circ$ in Stripe 82 region, in which $Decl.$ range photometry data have

similar seeing condition, number of repeat observations, and zero point with our one square degree field. We select all HST detected point sources within this area from Hubble Source Catalog (Whitmore et al. 2016) in HST Hubble Legacy Archive Release⁸. We then cross match ($1''$) them with Stripe 82 catalog to get the photometry data. Using the final point source sample, including ~ 2600 HST point sources, we calculate the fraction of how many point sources can be successfully classified as point source by our separation. It is a function of i band magnitude, as shown in Figure 6. The completeness is almost higher than 90% at i band magnitude brighter than 21 and drops to 75% to the magnitude limit ($i = 22.5$) of our survey. The average completeness within the magnitude limit is 92%, which is consistent with the selected fraction of previously known quasars (96/107) as discussed above.

To estimate the completeness of our color-color selection criteria, we generate a sample of simulated quasars following the procedure in Fan (1999a) and McGreer et al. (2013). Fan (1999a) described the procedure to generate simulated quasar spectra using an empirical model for quasar spectral properties at UV and optical wavelength. Based on simulated spectra, we can measure the simulated colors of each spectrum by integrating spectrum through bandpasses used by survey. Simulated colors can be used to define selection criteria and estimate the completeness of color cuts. McGreer et al. (2013) updated the spectral model of Fan (1999a) and applied it to higher redshift, assuming that the quasar spectral energy distributions do not evolve with redshift (Kuhn et al. 2001; Yip et al. 2004; Jiang et al. 2006). The quasar spectrum from (McGreer et al. 2013) is modeled as a power law continuum with a break at 1100\AA . They used normal distributions to describe the continuum slopes. The distribution of the blue side is $\mu(\alpha) = -1.7$ and $\sigma(\alpha) = 0.3$ (Telfer et al. 2002); the distribution of the red slope is $\mu(\alpha) = -0.5$ and $\sigma(\alpha) = 0.3$. Emission lines have been added to continuum using Gaussian profiles. The Gaussian parameters are also drawn from normal distributions which are generated from fitting composite spectra of quasars from the BOSS survey in different luminosity bins. We added breaks at 5700\AA and 9730\AA for redder wavelength coverage (in J, K bands), following the similar procedures in Yang et al. (2016). The slope (α_ν) from 5700\AA to 9730\AA follows a Gaussian distribution of $\mu(\alpha) = -0.48$ and $\sigma(\alpha) = 0.3$; the redder range continuum has a slope with the distribution of $\mu(\alpha) = -1.74$ and $\sigma(\alpha) = 0.3$ (Glikman et al. 2006). The parameters of emission lines are derived from the composite quasar spectra (Glikman et al. 2006).

The intergalactic medium absorption model used for our simulation is the same as McGreer et al. (2013), which extend the Ly α forest model based on the work of Worseck & Prochaska (2011) to higher redshift by using the observed number densities of high column density systems (Songaila & Cowie 2010). Compared to McGreer et al. (2013), we also made minor modifications for Fe emission. We use the template from Vestergaard & Wilkes (2001) for wavelengths shorter than 2200\AA . For $2200\text{-}3500\text{\AA}$, we use the template from Tsuzuki et

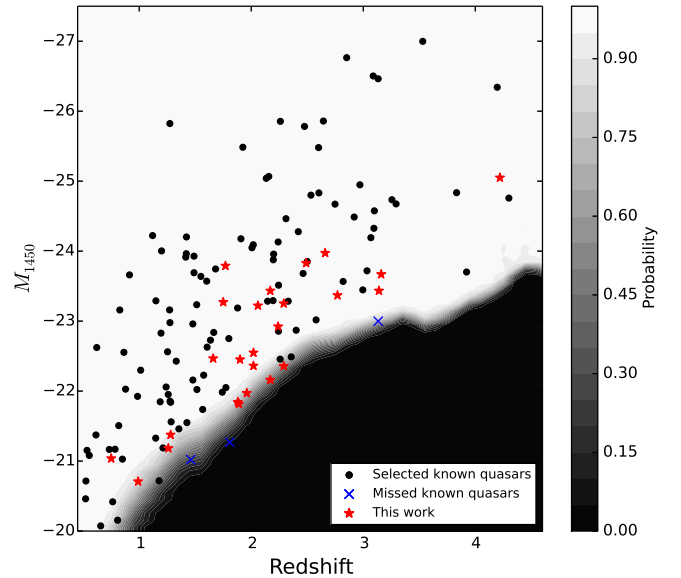


Fig. 7.— Selection function of color-color selection criteria. All 110 Stripe 82-Y-UDXS detected known quasars are denoted by black filled circles and blue crosses, for selected and missed known quasars, respectively. Red stars represent our new discoveries. Our selections show a very high completeness at the full redshift range from $z = 0.5$ to 4.5 . The completeness drops quickly at the bottom-right region, which is only caused by the magnitude limit ($i < 22.5$) of our survey. All of three missed quasars are rejected by this magnitude limit. At the bright end, there should be a small region out of the magnitude range ($17 < i < 23.1$) of simulation sample (See fig.8 also). But, for plot, here we also set the completeness value in this region to 1.0 since based on the selection function in nearby area our color selections can be expected to be continuous and keep the high completeness.

al. (2006) which separates the FeII emission from the MgII $\lambda 2798$ line. A template from Boroson & Green (1992) covering $3500\text{-}7500\text{\AA}$ is also added. The photometric datasets we used in optical and Y bands are from different surveys, and thus have different depths, with that were used by McGreer et al. (2013). Therefore, we need to simulate photometric uncertainties of Stripe 82 u, g, r, i, z photometry and our Y-band data. We use a sample of Stripe 82 classified point sources to fit the magnitude - error relations in u, g, r, i, z and Y bands. Using the simulation model and new magnitude - error relations, we generate photometric data of 1,085,800 simulated quasar spectra, evenly distributed in the (i, z) space. We construct a grid of quasars in the redshift range of $0.5 < z < 4.95$ and the magnitude range of $17 < i < 23.1$ to match the magnitude and redshift ranges of our quasar sample. There are ~ 200 quasars in each (i, z) bin with $\Delta m = 0.1$ and $\Delta z = 0.05$.

Based on the simulated quasar sample, we calculate the fraction of simulated quasars selected by our selection criteria as the selection probability, shown in Figure 7. We calculate the probability in each (M_{1450}, z) bin in the range of $-28 < M_{1450} < -20$ and $0.5 < z < 4.95$ with $\Delta M = 0.1$ and $\Delta z = 0.1$. As shown in Figure 7, our color-color selection criteria is highly complete at the magnitude range brighter than our magnitude limit ($i < 22.5$). It is consistent with the selection fraction of known quasars: all of three missed known quasars

⁸ <http://archive.stsci.edu/hst/hsc/>

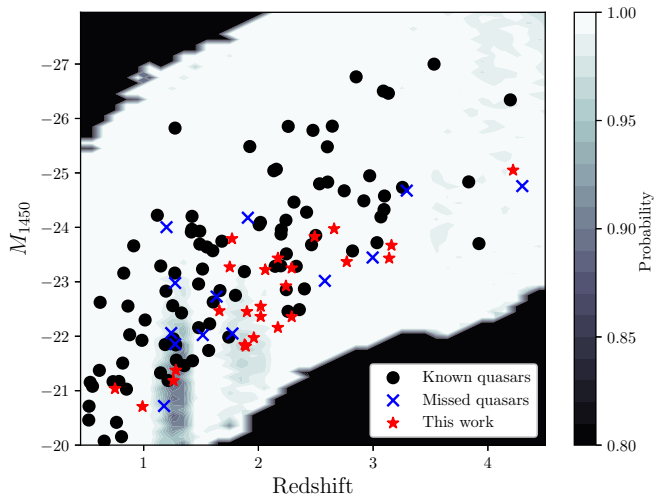


FIG. 8.— The completeness of $\chi^2 < 15$ limit in the magnitude range of $17 < i < 23.1$. The two dark regions are out of the magnitude range. Red stars represent our new discoveries. All previously known quasars are denoted by black filled circles and blue crosses, for selected and missed quasars, respectively. Considering more than 99.85% points show a completeness higher than 83.3%, here we scale the color bar to 0.8-1.0.

are only rejected by i band magnitude limit. Using this simulated quasar sample, we also calculate the incompleteness of χ^2 fitting. We calculate χ^2 value of each simulated quasar using the same method that we used for candidates selection. We generate the selection probability of χ^2 limit in (M_{1450}, z) space using the same bins as discussed above. The completeness of χ^2 estimator is plotted in Figure 8. When we constructed the color- z relation for χ^2 , to make the color- z accurate we reject quasars out of 3σ to the mean values of colors. The simulation method also does not include unusual weak line quasar and broad absorption line quasar. Therefore, quasars with extreme colors will not be covered by both simulation quasar sample and χ^2 estimator. Thus we will get a higher completeness of χ^2 limit than truth by using the simulation quasar sample. The difference will be smaller than the uncertainties of QLF measurement. We finally estimate the spectroscopy incompleteness by assuming the same fraction of quasars in observed and unobserved candidates sub-samples. Since when we did fiber allocation, we chose a configuration that could target more rank 1 candidates, here we estimate the spectroscopy incompleteness of each rank respectively. The spectroscopy completeness of quasars in rank 1 is 67%, while it is 33% and 30% for rank 2 and rank 3 quasars, respectively.

5. QLF IN ONE SQUARE DEGREE FIELD

To draw the distribution of quasars at different redshifts and magnitudes in this one square degree field, we calculate the QLF using this quasar sample including 109 quasars. We calculate the binned luminosity function by using the Page & Carrera (2000) implementation of the traditional $1/V_{\max}$ method (Schmidt 1968; Avni & Bahcall 1980) for flux limit correction. We divide our sample into 8 redshift bins at $0.5 < z < 4.5$ ($\Delta z = 0.5$) and 7 M_{1450} magnitude bins at $-27 < M_{1450} < -20$

($\Delta M = 1$). Since our quasar sample in a small area only includes 109 quasars but covers a wide redshift and magnitude range, if we use smaller magnitude bin, there will be one or two quasars in each bin, leading to large uncertainties of binned QLF. We prefer to focus on the redshift evolution and thus choose a large magnitude interval with $\Delta M = 1$ mag. We correct the incompleteness of our selection as discussed above. The binned data are listed in Table 2 and plotted in Figure 9. Considering the small quasar sample size in each $M_{1450} - z$ bin, we use mean value of redshift and M_{1450} .

Since our quasar sample cover a wide redshift range, we also measure the parametric QLF to discuss the evolution model of QLF with redshift. We model the parametric QLF following the double power law form (Boyle et al. 2000):

$$\Phi(M, z) = \frac{\Phi^*(z)}{10^{0.4(\alpha+1)(M-M^*)} + 10^{0.4(\beta+1)(M-M^*)}} \quad (9)$$

where α and β are the faint end and the bright end slopes; M^* is the break magnitude and $\Phi^*(z)$ is the normalization. We use the χ^2 fitting to fit binned QLF data at each redshift bin with the double power law formula. Our sample only covers the faint end of each redshift bin, so we fix the bright end slope β and break magnitude M_{1450}^* . Previous works have show strong evidence of a pure luminosity evolution (PLE) model of QLF at $z \lesssim 2.2$ and a luminosity evolution and density evolution (LEDE) model of QLF at $z \gtrsim 2.2$ Croom et al. (2009); Ross et al. (2013); Palanque-Delabrouille et al. (2013, 2016). Croom et al. (2009) used a sample of quasars from 2dF-SDSS LRG and QSO (2SLAQ) survey to derive the QLF at $0.4 < z < 2.6$. The PLE model used by Croom et al. (2009) shows the redshift dependence through the evolved break magnitude, described by

$$M^*(z) = M^*(0) - 2.5(k_1 z + k_2 z^2) \quad (10)$$

For bins at $z < 2.5$, we choose the same formula of the PLE model from Croom et al. (2009), and thus fix the bright end slope β and break magnitude M_{1450}^* to their result.

At $z > 2.5$, we choose the LEDE model from Ross et al. (2013). Ross et al. (2013) used the BOSS color selected DR9 quasar sample and BOSS Stripe 82 variability selected quasar sample to measure the QLF at $2.2 < z < 3.5$, and conclude that the QLF can be described well by an LEDE model, which is in a log-linear formula

$$\log[\Phi^*(z)] = \log[\Phi^*(z = 2.2)] + c_1(z - 2.2), \quad (11)$$

$$M_{i,2}^*(z) = M_{i,2}^*(z = 2.2) + c_2(z - 2.2) \quad (12)$$

We also fix β and M_{1450}^* to the result given by Ross et al. (2013). Because in our sample there are only few luminous quasars in each bin at the bright end, the bright end slopes will be highly uncertain due to small number statistics. Therefore, when we do the fitting, at each redshift bin, we reject binned QLF data in the magnitude bins that are brighter than the break magnitude. We do not do the fitting for bins at $z > 3.5$ since there are also only few quasars. The best-fits at different bins are summarized in Table 2.

In Figure 9, we plot our best-fit QLFs, comparing with binned QLF and QLFs at different redshifts from pre-

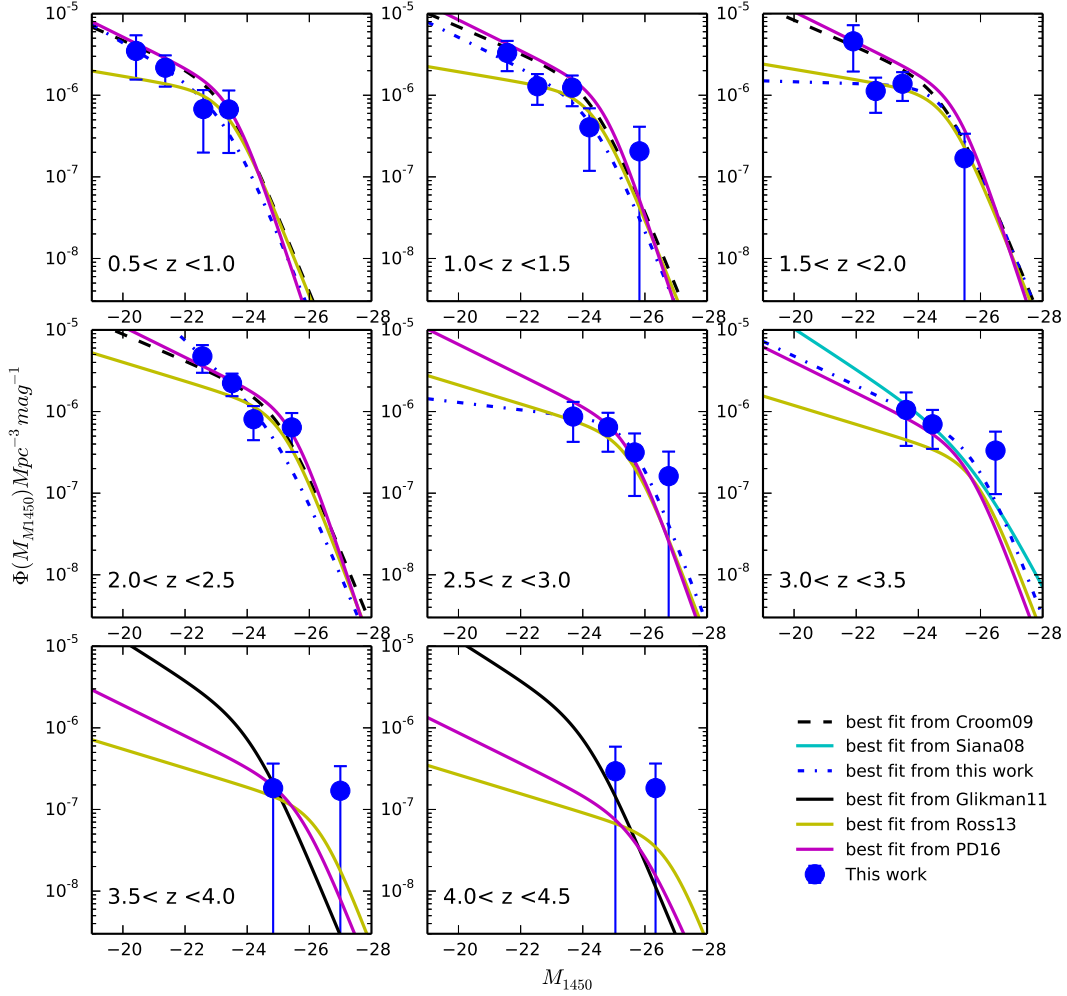


FIG. 9.— The binned (blue filled circle with error bars) and best-fits (blue dashed line) QLFs from our quasar sample. As a comparison, we plot QLFs from previous works at different redshifts. We compare our QLFs with the best-fit QLFs from Croom et al. (2009) at bins with $z < 2.5$ (black dashed lines), Ross et al. (2013) (yellow solid lines) with a PLE model at bins with $z < 2$ and a LEDE model at $z > 2$ (using parameters from Stripe 82 sample), Palanque-Delabrouille et al. (2016) (purple solid lines) in the full redshift range, the $z \sim 3$ QLF from Siana et al. (2008) (cyan lines) at redshift bin $3 < z < 3.5$ and the $z \sim 4$ QLF from Glikman et al. (2011) (black solid lines) at bins with $3.5 < z < 4.5$. We have converted the magnitudes used in their QLFs into M_{1450} and the cosmology into our adopted cosmology.

vious works (Croom et al. 2009; Glikman et al. 2011; Palanque-Delabrouille et al. 2016; Ross et al. 2013; Siana et al. 2008). The result from Croom et al. (2009) focused on the redshift range of $z < 2.6$, so we plot their QLF at bins of $z < 2.5$. Ross et al. (2013) concentrated on the redshift range of $2.2 < z < 3.5$, using both 23300 color selected quasars and 5476 variability selected quasars at $2.2 < z < 3.5$, and supplemented it with a deeper dataset over a smaller area to probe lower redshift at $0.7 < z < 2.2$. So we plot their result with PLE model at $z < 2.2$ and LEDE model at $2.2 < z < 3.5$. We also plot their LEDE QLF at $z > 3.5$ as a comparison, since the LEDE model with log-linear manner has also been suggested by the studies of high redshift QLF (e.g. McGreer et al. 2013; Yang et al. 2016). Palanque-Delabrouille et al. (2016) used the variability selected quasar sample in Stripe 82 area from SDSS-IV/eBOSS to present a de-

termination of QLF at $0.6 < z < 4$. Their data could be described well by both PLE and PLE ($z < 2.2$) + LEDE ($z > 2.2$) model. Here we plot the PLE+LEDE model from Palanque-Delabrouille et al. (2016). They adopted the same PLE formula to Croom et al. (2009) and a similar log-linear LEDE model with Ross et al. (2013) but required the QLF to be continuous at the pivot redshift ($z_p = 2.2$). As shown, our binned QLF and best-fits show agreement well with the PLE model used by Croom et al. (2009); Palanque-Delabrouille et al. (2016) at $z < 2.5$. At $2.5 < z < 3.5$, our QLF is following the LEDE model and is more consistent with Palanque-Delabrouille et al. (2016). We also plot the $z \sim 3.2$ QLF from the Spitzer Wide-area Infrared Extragalactic (SWIRE) survey (Siana et al. 2008; SWIRE+SDSS) and $z \sim 4$ QLF from NOAO Deep Wide-Field Survey (NDWFS) + Deep Lens Survey (DLS) (Glikman et al.

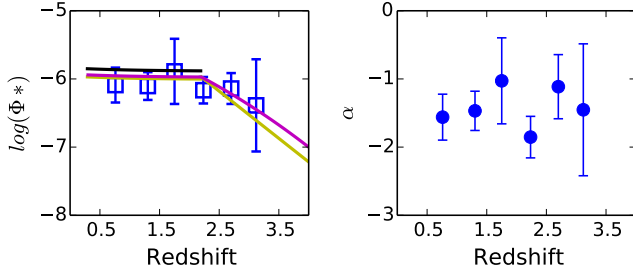


FIG. 10.— Parameters evolution, $\log(\Phi^*)$ (left) and the faint end slope α (right). The yellow and black solid lines represent the PLE + LEDE evolution model from Ross et al. (2013) and PLE model given by Croom et al. (2009). The PLE+LEDE model from Palanque-Delabrouille et al. (2016) is also shown as comparison (purple line).

2011) at bins with $3.0 < z < 3.5$ and $3.5 < z < 4.5$ respectively. At $z \sim 3$, the QLF from Siana et al. (2008) is included in the 1σ region of our binned data. At $z \sim 4$, our data have uncertainties too large to constraint the QLF. We show the $\log(\Phi^*)$ and the faint end slope α of best-fits versus redshift in Figure 10. Although our result is based on a small sample, the parameters evolution still can show the trend that $\log(\Phi^*)$ evolved with increasing redshift by a PLE model at lower redshift and a LEDE model at higher redshift. The faint end slope does not obviously evolve.

6. SUMMARY

In this work, we used deep CFHT Y-band image, deep optical data from SDSS Stripe 82 and NIR data from

UKIDSS DXS DR9 to survey quasars in a one square degree field. We used the color-color selection criteria $Y - K/g - z$ and $J - K/i - Y$ (Wu & Jia 2010) to select quasar candidates and discovered 25 new quasars at redshift range of $0.5 < z < 4.3$, which make obvious contribution to the quasars distribution of both $2 < z < 3$ and faint quasars in this field. By combining our new quasars and previously known quasars that meet our selection pipeline, we construct a quasar sample including 109 quasars in a 1.02 deg^2 field. We estimate the completeness of our selection pipeline using a sample of simulated quasars. It confirms that the $Y - K/g - z$ and $J - K/i - Y$ color-color cuts are highly complete at $z < 4.5$: all quasars within the magnitude limit can be selected by color-color criteria. We calculate the QLFs, both binned and parametric QLFs. The results show agreements with the PLE evolution model at $z < 2.5$ and the LEDE evolution at $z > 2.5$.

This optical+NIR color selection, yielding a high completeness at the wide redshift range of $z < 4.5$, can be applied for large area quasar survey to provide large complete quasar sample, especially for $2 < z < 3$ quasars. This method has already been used by the Large Sky Area Multi-Object Fiber Spectroscopic Telescope (LAMOST) quasar survey (Ai et al. 2016, ;X. Dong 2017 in prep) in the entire SDSS-ULAS area. More than 2500 new quasars have been discovered by using this selection. The new optical and NIR surveys with wide sky coverage, e.g. Pan-STARRS 1 (PS1; Chambers et al. 2016), the VLT Survey Telescope ATLAS survey (Shanks et al. 2015) and the VISTA Hemisphere Survey (VHS; McMahon et al. 2013), will offer perfect optical+NIR photometric dataset for a complete $z < 4.5$ quasar survey as well.

TABLE 1
QUASAR SAMPLE IN ONE SQUARE DEGREE FIELD

Name	Redshift	Ref_z	M_{1450}	g	i	z	Y	J	K
J221801.63+000041.18	1.665	SDSS	-22.84	21.21±0.012	20.96±0.018	20.91±0.076	20.43±0.026	19.67±0.027	18.59±0.030
J221805.79+000912.38	1.878	VVDS	-23.19	21.46±0.014	20.94±0.017	20.82±0.068	20.43±0.024	19.79±0.028	18.45±0.026
J221806.61+000535.08	2.310	SDSS	-24.46	20.24±0.006	20.21±0.009	19.96±0.032	19.45±0.009	19.25±0.020	17.87±0.017
J221806.68+005223.73	1.273	SDSS	-25.82	17.36±0.001	17.26±0.001	17.34±0.003	17.00±0.003	16.78±0.005	15.74±0.004
J221807.92+005229.82	3.095	SDSS	-24.33	21.52±0.016	21.13±0.023	21.19±0.084	20.66±0.026	20.13±0.033	19.34±0.052
J221809.38+004133.48	1.660	This work	-22.47	21.78±0.017	21.33±0.024	21.23±0.070	20.70±0.027	20.11±0.032	18.55±0.027
J221810.33+005017.19	1.606	SDSS	-22.63	21.51±0.015	21.08±0.021	21.20±0.083	20.67±0.029	20.06±0.031	18.59±0.028
J221812.92+002628.39	1.259	SDSS	-21.95	21.94±0.021	21.09±0.021	21.03±0.062	20.34±0.018	19.80±0.027	18.35±0.024
J221813.42+004854.03	2.357	VVDS	-22.49	23.06±0.054	22.24±0.057	21.88±0.130	21.21±0.038	20.87±0.055	19.65±0.068
J221814.21+002049.66	1.513	SDSS	-23.23	20.46±0.006	20.31±0.009	20.33±0.041	19.78±0.030	19.50±0.022	18.22±0.022
J221814.58+002736.82	2.240	SDSS	-24.13	20.76±0.008	20.47±0.012	20.18±0.029	19.60±0.013	19.38±0.021	17.92±0.018
J221815.32+000117.65	2.533	SDSS	-24.80	20.26±0.006	20.12±0.009	19.90±0.031	19.16±0.008	19.06±0.018	17.82±0.017
J221816.22+005848.36	1.330	SDSS	-22.43	20.88±0.017	20.76±0.040	20.45±0.063	19.59±0.020	19.29±0.019	17.88±0.016
J221816.60+000701.30	1.742	VVDS	-21.98	22.98±0.061	21.94±0.054	21.60±0.139	20.53±0.026	20.09±0.035	18.50±0.027
J221822.67+001715.32	0.524	VVDS	-20.71	20.41±0.006	19.98±0.007	19.91±0.028	19.72±0.013	18.82±0.015	17.79±0.017
J221825.03+002426.56	0.913	SDSS	-23.66	18.67±0.004	18.52±0.005	18.49±0.015	17.64±0.003	16.69±0.005	16.11±0.006
J221829.05+002024.14	1.479	VVDS	-22.16	21.77±0.017	21.32±0.022	21.30±0.099	20.35±0.039	20.09±0.032	18.52±0.026
J221830.06+000005.07	3.256	SDSS	-24.73	21.22±0.012	20.85±0.016	20.86±0.059	20.12±0.020	19.50±0.024	18.46±0.026
J221832.76+002424.94	1.890	This work	-21.82	23.27±0.065	22.32±0.055	21.99±0.187	21.09±0.037	20.36±0.038	18.78±0.032
J221833.31+001835.06	1.147	VVDS	-21.33	21.87±0.019	21.46±0.026	21.38±0.107	20.70±0.036	20.70±0.048	18.53±0.027
J221833.73+002709.46	1.253	VVDS	-22.56	20.77±0.008	20.47±0.012	20.38±0.035	19.64±0.009	19.24±0.019	17.68±0.015
J221835.26+004839.16	2.290	This work	-22.36	22.61±0.036	22.29±0.061	22.05±0.152	21.32±0.057	21.15±0.068	19.57±0.056
J221835.89+000342.44	3.068	SDSS	-24.19	21.35±0.015	21.24±0.023	21.15±0.098	20.44±0.025	20.08±0.036	18.80±0.036
J221839.12+004945.40	1.280	SDSS	-21.84	21.58±0.015	21.25±0.024	21.35±0.081	20.60±0.026	20.27±0.036	18.92±0.033
J221840.14+010038.52	2.970	SDSS	-24.95	20.56±0.008	20.40±0.013	20.45±0.048	19.79±0.024	19.59±0.023	18.57±0.027
J221841.02+005311.01	3.140	This work	-23.43	22.59±0.040	22.05±0.054	22.00±0.178	21.04±0.035	20.46±0.040	19.42±0.049
J221845.94+000953.06	2.258	SDSS	-22.46	22.22±0.030	22.15±0.053	22.08±0.227	21.27±0.066	21.06±0.074	19.37±0.056
J221852.62+005740.39	2.401	SDSS	-22.87	21.98±0.025	21.91±0.051	21.56±0.126	21.21±0.042	20.74±0.050	19.23±0.045
J221854.26-000058.75	3.099	SDSS	-24.58	21.14±0.012	20.88±0.016	20.69±0.050	20.31±0.033	19.50±0.024	18.37±0.025
J221854.37+002656.97	0.733	SDSS	-21.17	20.61±0.007	20.41±0.012	20.08±0.027	19.63±0.011	19.10±0.018	17.38±0.013
J221858.90+000712.21	3.034	VVDS	-23.72	22.42±0.036	21.68±0.035	21.51±0.133	20.66±0.027	20.51±0.049	19.37±0.056

TABLE 1 — *Continued*

Name	Redshift	Ref_z	M_{1450}	g	i	z	Y	J	K
J221859.21+003927.50	1.489	SDSS	-23.69	20.15±0.005	19.81±0.006	19.88±0.021	19.08±0.011	18.99±0.017	17.75±0.016
J221900.65+000812.26	1.415	SDSS	-23.91	19.67±0.004	19.45±0.005	19.54±0.022	19.24±0.010	18.67±0.015	17.57±0.015
J221901.41+000610.72	0.863	SDSS	-22.55	19.73±0.004	19.47±0.005	19.32±0.019	18.72±0.006	17.77±0.009	16.85±0.010
J221901.87+000025.92	1.149	SDSS	-23.29	19.75±0.004	19.51±0.005	19.51±0.023	19.09±0.009	18.66±0.015	17.36±0.013
J221907.94+004023.48	0.614	SDSS	-21.37	20.32±0.005	19.74±0.006	19.71±0.018	18.59±0.012	18.55±0.014	17.01±0.010
J221910.54+005606.50	1.195	SDSS	-22.83	20.59±0.007	20.07±0.009	20.16±0.033	19.56±0.032	19.18±0.018	18.00±0.016
J221912.11+00361300	0.826	SDSS	-23.16	18.72±0.002	18.75±0.003	18.65±0.008	18.79±0.018	17.49±0.008	16.48±0.008
J221912.60+000411.53	1.603	SDSS	-23.57	20.49±0.007	20.13±0.009	20.29±0.044	19.94±0.055	19.27±0.021	17.95±0.020
J221915.76+004232.7	2.170	This work	-23.43	21.18±0.010	21.08±0.019	20.79±0.046	20.18±0.019	20.18±0.036	18.60±0.029
J221924.27+004614.0	2.290	This work	-23.25	21.64±0.015	21.40±0.027	21.14±0.065	20.63±0.029	20.18±0.034	18.53±0.027
J221936.37+002434.12	2.852	SDSS	-26.76	18.63±0.002	18.48±0.002	18.45±0.008	17.84±0.004	17.35±0.007	16.60±0.007
J221937.14+001448.02	2.020	This work	-22.36	22.08±0.023	21.96±0.040	21.97±0.182	21.63±0.071	21.16±0.077	19.98±0.082
J221939.68+000809.7	1.960	This work	-21.97	22.46±0.035	22.26±0.056	22.36±0.285	21.45±0.089	21.08±0.072	19.84±0.073
J221941.99+003631.66	1.260	This work	-21.18	22.16±0.025	21.86±0.041	21.48±0.093	20.73±0.040	20.59±0.054	18.67±0.030
J221942.28+003253.12	2.018	SDSS	-24.09	20.29±0.006	20.23±0.010	20.03±0.025	19.49±0.014	19.52±0.025	18.44±0.025
J221942.46+003415.38	1.551	SDSS	-23.64	20.14±0.005	19.97±0.008	20.10±0.027	19.82±0.016	19.38±0.023	18.07±0.019
J221943.30+004118.38	3.133	SDSS	-26.46	19.45±0.003	19.03±0.003	19.02±0.010	18.38±0.006	17.85±0.009	16.80±0.008
J221945.08+003708.25	3.531	SDSS	-27.00	19.76±0.004	18.81±0.003	18.76±0.009	18.69±0.007	17.89±0.009	16.75±0.008
J221946.66+004340.76	1.800	SDSS	-22.75	21.48±0.020	21.26±0.032	21.26±0.081	20.40±0.027	20.16±0.039	18.80±0.034
J221946.92+000615.78	2.020	This work	-22.55	21.59±0.017	21.77±0.036	21.36±0.114	20.59±0.029	20.77±0.057	19.28±0.045
J221947.10+005526.29	2.146	SDSS	-23.28	21.37±0.013	21.20±0.024	20.92±0.064	20.41±0.030	19.98±0.030	18.56±0.028
J221951.27+004135.30	0.656	VVDS	-20.07	21.86±0.018	21.21±0.022	21.07±0.059	20.26±0.020	19.93±0.033	18.40±0.025
J221952.07+000054.21	0.817	SDSS	-21.51	20.53±0.007	20.37±0.010	20.13±0.038	19.93±0.019	18.82±0.016	17.45±0.012
J221952.12+001933.34	0.807	SDSS	-20.15	21.86±0.019	21.69±0.031	21.53±0.120	21.11±0.057	20.24±0.042	19.05±0.042
J221955.48+004722.78	1.770	This work	-23.79	20.63±0.007	20.17±0.009	20.20±0.028	19.69±0.014	19.28±0.019	18.22±0.021
J221957.22+005521.46	1.925	SDSS	-25.48	19.06±0.002	18.71±0.003	18.58±0.008	18.21±0.005	17.76±0.009	16.63±0.007
J221958.21+003709.33	3.089	SDSS	-26.50	19.21±0.003	18.95±0.004	18.97±0.010	18.48±0.006	18.00±0.010	17.10±0.010
J221958.42+001629.89	2.244	VVDS	-23.51	21.33±0.012	21.09±0.018	20.89±0.068	20.49±0.023	20.02±0.033	18.63±0.027
J222000.42+002137.83	1.271	SDSS	-23.16	20.19±0.005	19.91±0.007	20.04±0.031	19.19±0.010	19.07±0.019	17.62±0.014
J222001.31+000349.28	1.422	SDSS	-24.20	19.35±0.003	19.17±0.004	19.30±0.018	18.90±0.008	18.44±0.013	17.22±0.010
J222001.57+001222.69	2.770	This work	-23.37	21.98±0.022	21.79±0.036	21.70±0.156	21.45±0.060	20.81±0.058	19.68±0.064
J222002.85+004149.77	2.330	SDSS	-23.28	21.22±0.018	21.42±0.063	21.23±0.093	21.38±0.061	20.45±0.049	18.92±0.037
J222007.77+002332.06	2.420	SDSS	-24.28	21.37±0.012	20.52±0.011	20.17±0.035	19.42±0.012	18.99±0.018	17.67±0.014
J222012.53+001051.6	1.479	VVDS	-22.96	20.70±0.007	20.52±0.012	20.50±0.051	19.98±0.017	19.35±0.022	17.82±0.015
J222014.44+001859.16	2.490	This work	-23.83	20.97±0.009	21.05±0.017	20.62±0.052	20.16±0.023	19.52±0.025	18.22±0.022
J222014.59+004238.23	1.900	This work	-22.45	21.98±0.021	21.70±0.034	21.69±0.106	20.83±0.034	20.25±0.041	18.95±0.041
J222015.45+002601.46	2.243	SDSS	-22.86	22.06±0.024	21.75±0.036	21.48±0.091	20.76±0.040	20.36±0.044	18.74±0.033
J222020.40+001047.71	1.489	SDSS	-23.93	19.95±0.004	19.57±0.005	19.61±0.023	19.07±0.012	18.54±0.013	17.53±0.013
J222028.54+000531.63	2.748	SDSS	-24.67	21.08±0.010	20.47±0.011	20.15±0.037	19.26±0.011	18.99±0.017	17.78±0.015
J222029.53+004401.32	0.621	SDSS	-22.62	18.56±0.002	18.52±0.002	18.61±0.007	17.57±0.005	17.59±0.008	16.09±0.005
J222032.50+002537.66	4.196	SDSS	-26.34	21.90±0.021	21.91±0.007	19.87±0.021	19.13±0.010	18.75±0.015	17.41±0.012
J222034.37+005723.4	2.170	This work	-22.16	22.40±0.033	22.34±0.069	21.95±0.164	21.36±0.049	21.14±0.069	19.21±0.042
J222035.99+005339.3	1.426	VVDS	-21.55	22.86±0.049	21.83±0.042	21.71±0.128	20.86±0.035	20.12±0.034	18.49±0.025
J222037.15+001426.72	1.880	This work	-21.84	22.39±0.030	22.28±0.052	21.95±0.179	20.97±0.039	20.88±0.062	19.52±0.060
J222040.96+000531.41	2.500	SDSS	-23.85	21.10±0.011	21.04±0.019	20.83±0.069	20.47±0.031	20.17±0.037	18.48±0.025
J222043.88+002354.31	0.521	SDSS	-20.46	20.35±0.006	20.21±0.009	20.09±0.033	19.41±0.012	18.99±0.018	17.31±0.011
J222047.75+000853.08	0.985	SDSS	-21.92	21.02±0.010	20.45±0.011	19.94±0.031	19.30±0.011	18.56±0.014	17.06±0.009
J222050.60+005948.51	2.601	SDSS	-25.48	20.46±0.006	19.52±0.006	19.37±0.017	18.68±0.007	18.42±0.012	17.29±0.010
J222052.10+001024.92	2.463	SDSS	-23.68	21.41±0.014	21.17±0.021	20.85±0.070	20.35±0.025	20.00±0.033	18.47±0.025
J222052.76+004917.61	2.200	SDSS	-23.96	20.68±0.007	20.59±0.013	20.34±0.032	19.81±0.017	19.48±0.022	17.92±0.016
J222055.88+005219.41	2.604	SDSS	-24.83	20.14±0.005	20.16±0.960	19.92±0.025	19.62±0.012	19.26±0.020	18.05±0.018
J222057.44+000329.98	2.260	SDSS	-25.85	19.15±0.003	18.77±0.003	18.49±0.009	17.86±0.004	17.56±0.008	16.26±0.006
J222057.76+005105.25	1.013	SDSS	-22.30	20.29±0.006	20.15±0.009	20.06±0.028	19.45±0.014	18.93±0.016	17.47±0.012
J222058.98+005917.08	2.644	SDSS	-25.86	19.36±0.003	19.18±0.007	19.02±0.013	18.45±0.007	18.03±0.010	17.13±0.009
J222059.51+003840.95	2.820	VVDS	-23.57	22.80±0.044	21.64±0.032	21.35±0.078	20.53±0.030	20.03±0.035	18.65±0.032
J222100.33+005320.43	1.285	VVDS	-21.56	22.01±0.023	21.54±0.032	21.36±0.093	20.57±0.027	20.27±0.038	18.41±0.026
J222100.87+000950.97	1.354	VVDS	-21.46	22.08±0.025	21.78±0.036	21.47±0.122	20.55±0.036	20.41±0.044	18.88±0.035
J222103.42+005836.4	4.220	This work	-25.05	23.31±0.075	21.21±0.025	21.06±0.074	20.74±0.037	20.16±0.035	19.14±0.040
J222103.64+002203.46	1.187	VVDS	-21.85	21.26±0.011	21.04±0.017	20.81±0.063	20.21±0.021	19.83±0.029	18.33±0.022
J222103.80+004820.95	0.750	This work	-21.04	20.59±0.007	20.61±0.014	20.39±0.034	19.99±0.023	19.34±0.021	17.56±0.014
J222105.68+003101.83	3.160	This work	-23.67	22.32±0.032	21.84±0.042	21.69±0.111	21.08±0.047	20.50±0.044	18.63±0.027
J222110.30+002740.1	1.280	This work	-21.38	22.21±0.028	21.71±0.036	21.73±0.114	20.84±0.041	20.50±0.046	19.03±0.038
J222112.97+010115.88	2.006	SDSS	-24.05	20.43±0.007	20.25±0.033	20.14±0.151	19.32±0.047	19.62±0.025	18.36±0.022
J222118.57+001144.66	2.157	SDSS	-25.07	19.55±0.003	19.43±0.005	19.23±0.017	19.36±0.010	18.95±0.017	17.33±0.011
J222121.18+001247.36	2.240	This work	-22.92	22.25±0.027	21.67±0.030	21.44±0.114	20.71±0.034	20.66±0.055	19.18±0.044
J222126.96+001451.09	2.660	This work	-23.97	21.45±0.013	21.08±0.018	20.92±0.070	20.19±0.018	20.07±0.036	18.88±0.035
J222128.67+001443.58	1.682	VVDS	-23.75	20.34±0.010	20.08±0.026	20.13±0.065	19.53±0.014	19.11±0.019	17.90±0.016
J222128.71+004455.86	2.134	SDSS	-25.04	19.62±0.003	19.43±0.005	19.19±0.012	18.71±0.007	18.53±0.013	17.18±0.011
J222129.87+000430.07	2.476	SDSS	-25.78	19.15±0.002	19.08±0.004	18.88±0.012	18.30±0.005	18.02±0.010	16.83±0.008
J222132.56+010005.43	3.833	VVDS	-24.84	22.17±0.027	21.18±0.025	21.19±0.086	20.45±0.040	20.14±0.034	19.12±0.039
J222133.06+004040.36	2.197	SDSS	-23.88	20.83±0.008	20.67±0.014	20.41±0.034	20.34±0.051	19.70±0.026	18.24±0.020
J222136.96+001144.23	1.420	SDSS	-23.96	19.55±0.003	19.41±0.005	19.51±0.020	19.24±0.009	18.63±0.014	17.11±0.009
J222138.01+001559.6	2.060	This work	-23.22	21.26±0.011	21.15±0.019	21.00±0.076	20.82±0.041	20.17±0.038	19.02±0.039
J222143.21+002550.25	0.990	This work	-20.71	22.64±0.041	21.68±0.035	21.12±0.067	20.23±0.022	19.47±0.023	17.99±0.017
J222143.61+002456.41	1.119	SDSS	-24.22	18.57±0.002	18.51±0.002	18.54±0.009	17.98±0.006	17.92±0.010	16.67±0.007
J222146.13+003745.24	1.750	This work	-23.27	20.82±0.008	20.66±0.014	20.59±0.040	20.36±0.042	19.61±0.024	18.35±0.022
J222146.71+002303.91	2.195	SDSS	-23.29	21.41±0.013	21.25±0.022	21.08±0.082	20.65±0.041	20.41±0.043	18.77±0.031

TABLE 1 — *Continued*

Name	Redshift	Ref_z	M_{1450}	g	i	z	Y	J	K
J222150.92+001345.44	0.784	SDSS	-21.17	20.58±0.007	20.59±0.012	20.26±0.039	19.57±0.029	18.89±0.017	17.47±0.012

TABLE 2
BINNED QLF & PARAMETRIC QLF

redshift range	$\langle z \rangle$	M_{1450} bin	$\langle M_{1450} \rangle$	$\log(\Phi)$	σ_ϕ^a	$\log(\Phi^*)^c$	$\sigma_{\log(\Phi^*)}$	α	σ_α
0.5 < z < 1.0	0.760	-23.5	-23.410	-6.174	0.474	-6.090	0.256	-1.561	0.337
		-22.5	-22.588	-6.169	0.479				
		-21.5	-21.363	-5.662	0.902				
		-20.5	-20.422	-5.457	1.935				
1.0 < z < 1.5	1.303	-25.823 ^b	-25.823	-6.687	0.206	-6.104	0.204	-1.468	0.288
		-24.5	-24.212	-6.393	0.286				
		-23.5	-23.658	-5.907	0.506				
		-22.5	-22.539	-5.889	0.527				
		-21.5	-21.566	-5.481	1.331				
1.5 < z < 2.0	1.751	-25.485	-25.485	-6.772	0.169	-5.889	0.478	-1.028	0.631
		-23.5	-23.491	-5.859	0.533				
		-22.5	-22.627	-5.948	0.518				
		-21.5	-21.904	-5.339	2.629				
2.0 < z < 2.5	2.235	-25.5	-25.436	-6.194	0.320	-6.165	0.194	-1.853	0.305
		-24.5	-24.202	-6.094	0.361				
		-23.5	-23.511	-5.652	0.687				
		-22.5	-22.558	-5.323	1.766				
2.5 < z < 3.0	2.700	-26.765	-26.765	-6.792	0.162	-6.141	0.227	-1.114	0.470
		-25.5	-25.669	-6.501	0.223				
		-24.5	-24.813	-6.191	0.322				
		-23.5	-23.69	-6.061	0.444				
3.0 < z < 3.5	3.119	-26.5	-26.483	-6.478	0.235	-6.388	0.676	-1.453	0.968
		-24.5	-24.457	-6.156	0.349				
		-23.5	-23.607	-5.98	0.667				
3.5 < z < 4.0	3.682	-26.998	-26.998	-6.771	0.170	-	-	-	-
		-24.835	-24.835	-6.739	0.183				
4.0 < z < 4.5	4.208	-26.342	-26.342	-6.738	0.183	-	-	-	-
		-25.050	-25.050	-6.532	0.294				

^a σ_ϕ is in units of $10^{-6}\text{Mpc}^{-3}\text{mag}^{-1}\text{s}$.

^b For magnitude bins including only one quasar, we use the M_{1450} of this quasar.

^c The best fits at each redshift bin. Since we fix the bright end slope β and break magnitude M_{1450}^* to Croom et al. (2009) and Ross et al. (2013) at different redshift range, here we only list the best fits and uncertainties of $\log(\Phi^*)$ and α .

J. Y. and X.-B. W. thank the supports by the NSFC grant No.11373008 and 11533001, the Strategic Priority Research Program "The Emergence of Cosmological Structures" of the Chinese Academy of Sciences, Grant No. XDB09000000, the National Key Basic Research Program of China 2014CB845700, and from the Ministry of Science and Technology of China under grant 2016YFA0400703. D.-Z.L., S.Y., and Z.-H.F. acknowledge the support from NSFC of China under grants 11333001, 11173001, and 11033005, and from the Strategic Priority Research Program "The Emergence of Cosmological Structure" of the Chinese Academy of Science, grant no. XDB09000000. X.F. and I.D.M. ac-

knowledge the support from US NSF grant AST 15-15115 and NASA ADAP grant NNX17AF28G. H.-Y.S. acknowledges the support from TR33 project "The Dark Universe" funded by the DFG. This research uses data obtained through the Telescope Access Program (TAP), which has been funded by the Strategic Priority Research Program "The Emergence of Cosmological Structures" (Grant No. XDB09000000), National Astronomical Observatories, Chinese Academy of Sciences, and the Special Fund for Astronomy from the Ministry of Finance in China. We acknowledge the use of the CFHT and the MMT 6.5 m telescopes. This work was partially supported by the Open Project Program of the Key Laboratory of Optical Astronomy, National Astronomical Observatories, Chinese Academy of Sciences.

We acknowledge the use of SDSS photometric data. Funding for SDSS-III has been provided by the Alfred P. Sloan Foundation, the Participating Institutions, the National Science Foundation, and the U.S. Department of Energy Office of Science. The SDSS-III Web site is <http://www.sdss3.org/>. SDSS-III is managed by the Astrophysical Research Consortium for the Participat-

ing Institutions of the SDSS-III Collaboration including the University of Arizona, the Brazilian Participation Group, Brookhaven National Laboratory, University of Cambridge, Carnegie Mellon University, University of Florida, the French Participation Group, the German Participation Group, Harvard University, the Instituto de Astrofísica de Canarias, the Michigan State/Notre Dame/JINA Participation Group, Johns Hopkins University, Lawrence Berkeley National Laboratory, Max Planck Institute for Astrophysics, Max Planck Insti-

tute for Extraterrestrial Physics, New Mexico State University, New York University, Ohio State University, Pennsylvania State University, University of Portsmouth, Princeton University, the Spanish Participation Group, University of Tokyo, University of Utah, Vanderbilt University, University of Virginia, University of Washington, and Yale University. We acknowledge the use of the UKIDSS data and Hubble Source Catalog ⁹.

Facilities: Sloan (SDSS), UKIRT/WFCAM, CFHT/WIRCam, MMT/Hectospec.

REFERENCES

- Ai, Y. L., Wu, X.-B., Yang, J., et al. 2016, *AJ*, 151, 24
 Annis, J., Soares-Santos, M., Strauss, M. A., et al. 2014, *ApJ*, 794, 120
 Avni, Y., & Bahcall, J. N. 1980, *ApJ*, 235, 694
 Baldwin, J. A. 1977, *ApJ*, 214, 679
 Bertin, E., & Arnouts, S. 1996, *A&AS*, 117, 393
 Bongiorno, A., Zamorani, G., Gavignaud, I., et al. 2007, *A&A*, 472, 443
 Boroson, T. A., & Green, R. F. 1992, *ApJS*, 80, 109
 Boyle, B. J., Shanks, T., Croom, S. M., et al. 2000, *MNRAS*, 317, 1014
 Cardelli, J. A., Clayton, G. C., & Mathis, J. S. 1989, *ApJ*, 345, 245
 Casali, M., Adamson, A., Alves de Oliveira, C., et al. 2007, *A&A*, 467, 777
 Chambers, K. C., Magnier, E. A., Metcalfe, N., et al. 2016, *arXiv:1612.05560*
 Condon, J. J., Cotton, W. D., Greisen, E. W., et al. 1998, *AJ*, 115, 1693
 Croom, S. M., Smith, R. J., Boyle, B. J., et al. 2004, *MNRAS*, 349, 1397
 Croom, S. M., Richards, G. T., Shanks, T., et al. 2009, *MNRAS*, 399, 1755
 Dawson, K. S., Kneib, J.-P., Percival, W. J., et al. 2016, *AJ*, 151, 44
 Dawson, K. S., Schlegel, D. J., Ahn, C. P., et al. 2013, *AJ*, 145, 10
 Di Matteo, T., Springel, V., & Hernquist, L. 2005, *Nature*, 433, 604
 Garilli, B., Le Fèvre, O., Guzzo, L., et al. 2008, *A&A*, 486, 683
 Glikman, E., Djorgovski, S. G., Stern, D., et al. 2011, *ApJ*, 728, L26
 Glikman, E., Helfand, D. J., & White, R. L. 2006, *ApJ*, 640, 579
 Fabricant, D., Fata, R., Roll, J., et al. 2005, *PASP*, 117, 1411
 Fan, X. 1999a, *AJ*, 117, 2528
 Fan, X., Strauss, M. A., Schneider, D. P., et al. 1999b, *AJ*, 118, 1
 Hewett, P. C., Warren, S. J., Leggett, S. K., & Hodgkin, S. T. 2006, *MNRAS*, 367, 454
 Jiang, L., Fan, X., Cool, R. J., et al. 2006, *AJ*, 131, 2788
 Komatsu, E., Dunkley, J., Nolta, M. R., et al. 2009, *ApJS*, 180, 330
 Kuhn, O., Elvis, M., Bechtold, J., & Elston, R. 2001, *ApJS*, 136, 225
 Lawrence, A., Warren, S. J., Almaini, O., et al. 2007, *MNRAS*, 379, 1599
 Le Fèvre, O., Cassata, P., Cucciati, O., et al. 2013, *A&A*, 559, A14
 Liu, D., Yang, J., Yuan, S., et al. 2017, *AJ*, 153, 53
 Lupton, R. H., Gunn, J. E., & Szalay, A. S. 1999, *AJ*, 118, 1406
 Maddox, N., Hewett, P. C., Warren, S. J., & Croom, S. M. 2008, *MNRAS*, 386, 1605
 McGreer, I. D., Jiang, L., Fan, X., et al. 2013, *ApJ*, 768, 105
 McMahon, R. G., Banerji, M., Gonzalez, E., et al. 2013, *The Messenger*, 154, 35
 Myers, A. D., Palanque-Delabrouille, N., Prakash, A., et al. 2015, *ApJS*, 221, 27
 Page, M. J., & Carrera, F. J. 2000, *MNRAS*, 311, 433
 Palanque-Delabrouille, N., Magneville, C., Yèche, C., et al. 2013, *A&A*, 551, A29
 Palanque-Delabrouille, N., Magneville, C., Yèche, C., et al. 2016, *A&A*, 587, A41
 Pâris, I., Petitjean, P., Aubourg, É., et al. 2012, *A&A*, 548, A66
 Pâris, I., Petitjean, P., Aubourg, É., et al. 2014, *A&A*, 563, A54
 Pâris, I., Petitjean, P., Ross, N. P., et al. 2017, *A&A*, 597, A79
 Peterson, B. M. 1997, *An introduction to active galactic nuclei*, Publisher: Cambridge, New York Cambridge University Press, 1997 Physical description xvi, 238 p. ISBN 0521473489,
 Richards, G. T., Fan, X., Newberg, H. J., et al. 2002, *AJ*, 123, 2945
 Ross, N. P., McGreer, I. D., White, M., et al. 2013, *ApJ*, 773, 14
 Ross, N. P., Myers, A. D., Sheldon, E. S., et al. 2012, *ApJS*, 199, 3
 Schmidt, M. 1968, *ApJ*, 151, 393
 Schlegel, D. J., Finkbeiner, D. P., & Davis, M. 1998, *ApJ*, 500, 525
 Schneider, D. P., Fan, X., Hall, P. B., et al. 2003, *AJ*, 126, 2579
 Schneider, D. P., Hall, P. B., Richards, G. T., et al. 2007, *AJ*, 134, 102
 Schneider, D. P., Hall, P. B., Richards, G. T., et al. 2005, *AJ*, 130, 367
 Schneider, D. P., Richards, G. T., Hall, P. B., et al. 2010, *AJ*, 139, 2360
 Shanks, T., Metcalfe, N., Chehade, B., et al. 2015, *MNRAS*, 451, 4238
 Songaila, A., & Cowie, L. L. 2010, *ApJ*, 721, 1448
 Siana, B., Polletta, M. d. C., Smith, H. E., et al. 2008, *ApJ*, 675, 49-70
 Telfer, R. C., Zheng, W., Kriss, G. A., & Davidsen, A. F. 2002, *ApJ*, 565, 773
 Tsuzuki, Y., Kawara, K., Yoshii, Y., et al. 2006, *ApJ*, 650, 57
 Ueda, Y., Akiyama, M., Ohta, K., & Miyaji, T. 2003, *ApJ*, 598, 886
 Venemans, B. P., Findlay, J. R., Sutherland, W. J., et al. 2013, *ApJ*, 779, 24
 Vestergaard, M., & Wilkes, B. J. 2001, *ApJS*, 134, 1
 Wang, W.-H., Cowie, L. L., Barger, A. J., Keenan, R. C., & Ting, H.-C. 2010, *ApJS*, 187, 251
 Warren, S. J., Hewett, P. C., & Foltz, C. B. 2000, *MNRAS*, 312, 827
 Weinstein, M. A., Richards, G. T., Schneider, D. P., et al. 2004, *ApJS*, 155, 243
 Whitmore, B. C., Allam, S. S., Budavári, T., et al. 2016, *AJ*, 151, 134
 Worseck, G., & Prochaska, J. X. 2011, *ApJ*, 728, 23
 Wu, X.-B., Chen, Z.-Y., Jia, Z.-D., et al. 2010, *Research in Astronomy and Astrophysics*, 10, 737
 Wu, X.-B., Jia, Z.-D., Chen, Z.-Y., et al. 2010, *Research in Astronomy and Astrophysics*, 10, 745
 Wu, X.-B., & Jia, Z. 2010, *MNRAS*, 406, 1583
 Wu, X.-B., Wang, R., Schmidt, K. B., et al. 2011, *AJ*, 142, 78
 Yang, J., Wang, F., Wu, X.-B., et al. 2016, *ApJ*, 829, 33
 Yang, Q., Wu, X.-B., Fan, X., et al. 2017, *AJ*, 154, 269
 Yip, C. W., Connolly, A. J., Vanden Berk, D. E., et al. 2004, *AJ*, 128, 2603
 Yuan, H., Zhang, H., Zhang, Y., et al. 2013, *Astronomy and Computing*, 3, 65

⁹ Based on observations made with the NASA/ESA Hubble Space Telescope, and obtained from the Hubble Legacy Archive,

which is a collaboration between the Space Telescope Science Insti-

